Oxygen-Bridged Dual Catalytic Sites Enable Asymmetric C-C Coupling for Efficient CO_2 Electroreduction to Ethanol

Shifu Wang[1,2,‡], Jian Zhao[3,‡], Ouardia Akdim[4], Yaqiong Zeng[1], Xiyu Li[1], Weijue Wang[1], Ying-Rui Lu[5], Wei Xu[6,7], Xuning Li[1,*], Yanqiang Huang[1,2,*], Graham J. Hutchings[4,*], Bin Liu[8,9,*] and Tao Zhang[1]

[1]State Key Laboratory of Catalysis, Dalian Institute of Chemical Physics, Chinese Academy of Sciences, Dalian 116023, P. R. China

[2]Department of Chemical Physics, University of Science and Technology of China, Hefei 230026, P. R. China

[3]School of Chemistry and Chemical Engineering, Liaoning Normal University, Dalian 116029, P. R. China

[4]Max Planck-Cardiff Centre on the Fundamentals of Heterogeneous Catalysis FUNCAT, Cardiff Catalysis Institute, School of Chemistry, Cardiff University, Cardiff, United Kingdom

[5]National Synchrotron Radiation Research Center, Hsinchu 300, Taiwan

[6]Beijing Synchrotron Radiation Facility, Institute of High Energy Physics, Beijing 100049, P. R. China

[7]RICMASS, Rome International Center for Materials Science Superstripes, Via dei Sabelli 119A, Roma 00185, Italy

[8] Department of Materials Science and Engineering, City University of Hong Kong, Hong Kong SAR 999077, P. R. China

[9]Department of Chemistry, Hong Kong Institute for Clean Energy (HKICE) & Center of Super-Diamond and Advanced Films (COSDAF), City University of Hong Kong, Hong Kong SAR 999077, P. R. China

‡These authors contributed equally to this work

*Corresponding authors: lixn@dicp.ac.cn (X.L.), yqhuang@dicp.ac.cn (Y.H.), hutch@cardiff.ac.uk (G.H.) and bliu48@cityu.edu.hk (B.L.)

ABSTRACT

Understanding C-C coupling pathways is essential for achieving selective CO_2 conversion into multi-carbon products. However, controlling intermediates dimerization remains highly challenging due to both the complexity of the catalytic systems and the limited mechanistic knowledge into the C-C coupling process. In this work, a model dual-site catalyst with precisely configured Fe-O-Cu sites is designed by covalently grafting iron-phthalocyanine (FePc) onto copper nanowires *via* oxygen bridges (FeN_4-O-Cu NW), which enables probing of atomic-level mechanistic insights into the C-C coupling pathways during electrochemical CO_2 reduction reaction (CO_2RR). Remarkably, the FeN_4-O-Cu NW exhibits a 23.6-fold enhancement in the ethanol-to-ethylene Faradaic efficiency ratio as compared to O-Cu NW, achieving >80% C_{2+} Faradaic efficiency at an industrially relevant current density of 1 A cm^{-2}. $^{13}CO_2/^{12}CO$ co-feed experiments together with a collection of *operando*/*in-situ* characterizations reveal that the enhanced ethanol selectivity over FeN_4-O-Cu NW arises from asymmetric C-C coupling between *CO and *CHO intermediates, where *CO is generated at the low-spin single-Fe-atom site, while *CHO is produced at the oxygen-bridged Cu site. Density functional theory (DFT) calculations further unveil that the oxygen-bridged Fe-O-Cu site can not only stabilize the *in-situ* generated low-spin Fe(II) active site for enhancing CO_2 activation and lowering *CO desorption energy, but also construct an oxygen-bridged Cu active site to stabilize the *OCHO intermediate, significantly lowering the *OCHO-to-*CHO conversion energy barrier, orchestrating an efficient asymmetric *CO-*CHO coupling path and boosting the CO_2-to-ethanol conversion.

INTRODUCTION

Excessive fossil fuel consumption has significantly raised atmospheric CO_2 levels, underscoring the urgent demand for advanced technologies to efficiently convert and store renewable energy[1,2]. The electrochemical CO_2 reduction reaction (CO_2RR) stands out as a promising strategy for chemically storing intermittent renewable energy by converting CO_2 into value-added carbon-based fuels and chemicals[3-7]. Among the diverse products achievable *via* CO_2RR, multi-carbon (C_{2+}) compounds, particularly ethanol, have garnered significant attention due to their high energy density and versatile applications as chemical feedstocks, clean fuels, and pharmaceutical intermediates[8-13].

In this context, the design of electrocatalysts capable of efficiently and selectively reducing CO_2 to ethanol has emerged as a central focus in CO_2RR research[14-16]. However, achieving high ethanol selectivity remains a significant challenge, primarily due to the sluggish kinetics of carbon-carbon (C-C) coupling. This bottleneck arises from two main factors: firstly, the low surface coverage of adsorbed *CO diminishes the likelihood for C-C coupling to occur[17-19]. Secondly, the complex multiple CO_2RR pathways limits the CO_2-to-ethanol selectivity[20,21]. For instance, the thermodynamic instability of key coupling intermediates (*e.g.*, *COCHO, *COCOH, *COCO, *CH_2CO, and *$OCHCH_2$) leads to competing CO_2RR pathways that favor the production of C_1 products or HER[19,22-26]. Consequently, regulating the key intermediates involved in the CO_2RR over precisely designed catalytically active sites and optimizing their adsorption, desorption capabilities as well as configurations are critical to manipulating the C-C coupling pathways towards producing ethanol, but it remains a grand challenge.

Single-atom catalysts (SACs), featuring well-defined and atomically dispersed metal sites, represent a highly promising platform for the precise construction of model catalysts[27-29]. Through strategies like coordination environment regulation, alloying, and the design of inorganic-organic

interfaces, the binding strength between catalytic sites and target intermediate species can be optimized, providing new opportunities for controllable manipulation of the C-C coupling pathway[8,29-34]. For instance, Sargent *et al.* constructed a molecule-metal interface to create a local environment rich in *CO intermediate, thereby enhancing the electrosynthesis of ethanol[31]. Recently, Cuenya *et al.* elucidated the distinct pathways for CO_2RR to C_{2+} products through combined *in-situ* Raman spectroscopy measurements and DFT calculations, revealing that ethylene formed *via* *OC-CO(H) coupling on undercoordinated Cu sites, while ethanol production required compressed Cu domains with modified electronic states to stabilize the key *$OCHCH_2$ intermediate[9]. Despite significant progress, challenges remain under *operando* conditions, particularly in the precise identification of catalytic sites, the configuration of bonded intermediate species, and the exact C-C coupling mechanism. In our previous research, the enhanced ethanol selectivity observed in single-Ag-atom modified Cu nanowires was attributed to the promoted H_2O dissociation at atomically dispersed Ag sites, which could accelerate *CO hydrogenation to form *CHO intermediate and facilitate asymmetric *CO-*CHO coupling on adjacent paired Cu atoms[15]. Therefore, design of dual-site catalysts have emerged as a promising solution to tackle C-C coupling challenges by leveraging the synergistic interaction between two distinct active sites to better stabilize intermediates, promote dimerization reaction, and provide insights into the C-C coupling mechanism during CO_2RR to ethanol[35].

Herein, by covalently anchoring iron-phthalocyanine to copper nanowires *via* oxygen bridges (FeN_4-O-Cu NW), a model dual-site catalyst with well-defined Fe-O-Cu sites is developed to decipher the active structural features responsible for CO_2RR toward ethanol production and the underlying C-C coupling mechanism. Specifically, the FeN_4-O-Cu NW catalyst exhibits an exceptional CO_2RR performance, achieving a maximum ethanol Faradaic efficiency (FE) of 57.3% at -0.9 V *vs*. RHE with

an ethanol partial current density as high as 282.5 mA cm^{-2}, and over 80% Faradaic efficiency for C_{2+} products at an industrial current density of 1 A cm^{-2}. *Operando* X-ray absorption spectroscopy (XAS) and *operando* ^{57}Fe Mössbauer spectroscopy measurements reveal the dynamic evolution of catalytically active sites during the CO_2RR, showing gradual reduction of copper sites and transformation of single-Fe-atom sites from low-spin (LS) Fe(III) to LS Fe(II). *Quasi in-situ* XPS analysis discloses that the oxygen-bridged Fe-O-Cu configuration can effectively stabilize the Cu^+ species during CO_2 electrocatalysis. Additionally, $^{13}CO_2/^{12}CO$ co-feed experiments together with *operando* attenuated total reflectance surface enhanced infrared absorption spectroscopy (ATR-SEIRAS) measurements indicate that the enhanced ethanol selectivity over FeN_4-O-Cu NW arises from the favorable asymmetric C-C coupling between *CO and *CHO, where *CO is generated at the LS Fe(II) site, while *CHO is produced at the oxygen-bridged Cu site. Density functional theory (DFT) calculations further elucidate that the oxygen-bridged Fe-O-Cu catalytic sites can not only stabilize the *in-situ* generated LS Fe(II), thereby facilitating CO_2 activation and concurrently reducing *CO desorption, but also form highly synergistic O-Cu dual active site, able to stabilize the *OCHO intermediate, lowering the *OCHO-to-*CHO conversion energy barrier and thus orchestrating an efficient asymmetric *CO-*CHO coupling path.

RESULTS AND DISCUSSION

Catalyst synthesis and characterization

The oxygen-bridged dual-site electrocatalyst was synthesized through a wet chemical method (see Methods for details). Specifically, in the presence of trimethylamine, chlorophthalocyanine iron (Cl-FePc, Supplementary Fig. 1) was grafted onto hydroxylated copper nanowires via a reflux process, removing H-Cl to form the oxygen-bridged FeN_4-O-Cu NW catalyst. Fig. 1 illustrates the synthesis process, with additional experimental details provided in the Supplementary Methods. One-dimensional Cu nanowires (Cu NW) with an average diameter of 45 ± 3 nm were imaged using transmission electron microscopy (TEM) (Supplementary Fig. 2). Compared to pristine Cu NW, the FeN_4-O-Cu NW displays obviously rougher surface (Fig. 2a and Supplementary Fig. 3). High-angle annular dark-field scanning transmission electron microscopy (HAADF-STEM) image combined with energy-dispersive X-ray spectroscopy (EDX) elemental mapping demonstrates the absence of Fe clusters or nanoparticles in FeN_4-O-Cu NW, with isolated Fe atoms uniformly dispersed across the entire hydroxylated copper nanowires matrix (Figs. 2b, 2c and Supplementary Fig. 4). *Ex-situ* Fourier transform infrared (FT-IR) spectroscopy and Raman spectroscopy were employed to comprehensively verify the successful synthesis of chlorophthalocyanine iron molecules (Supplementary Figs. 5, 6 and Supplementary Tables 1, 2)[36,37]. Power X-ray diffraction (XRD) analysis provides further evidence for the bulk metallic Cu phase in the FeN_4-O-Cu NW (Supplementary Fig. 7). No characteristic peaks corresponding to Cl-FePc species are observed in the XRD pattern of FeN_4-O-Cu NW, suggesting a minimal Fe content. The Fe content in FeN_4-O-Cu NW was quantified to be 0.65 wt.% *via* inductively coupled plasma optical emission spectrometry (ICP-OES, Supplementary Table 3). A broad XRD peak at 36.5° (position 1) can be attributed to CuO_x resulting from the hydroxylation treatment of Cu NW.

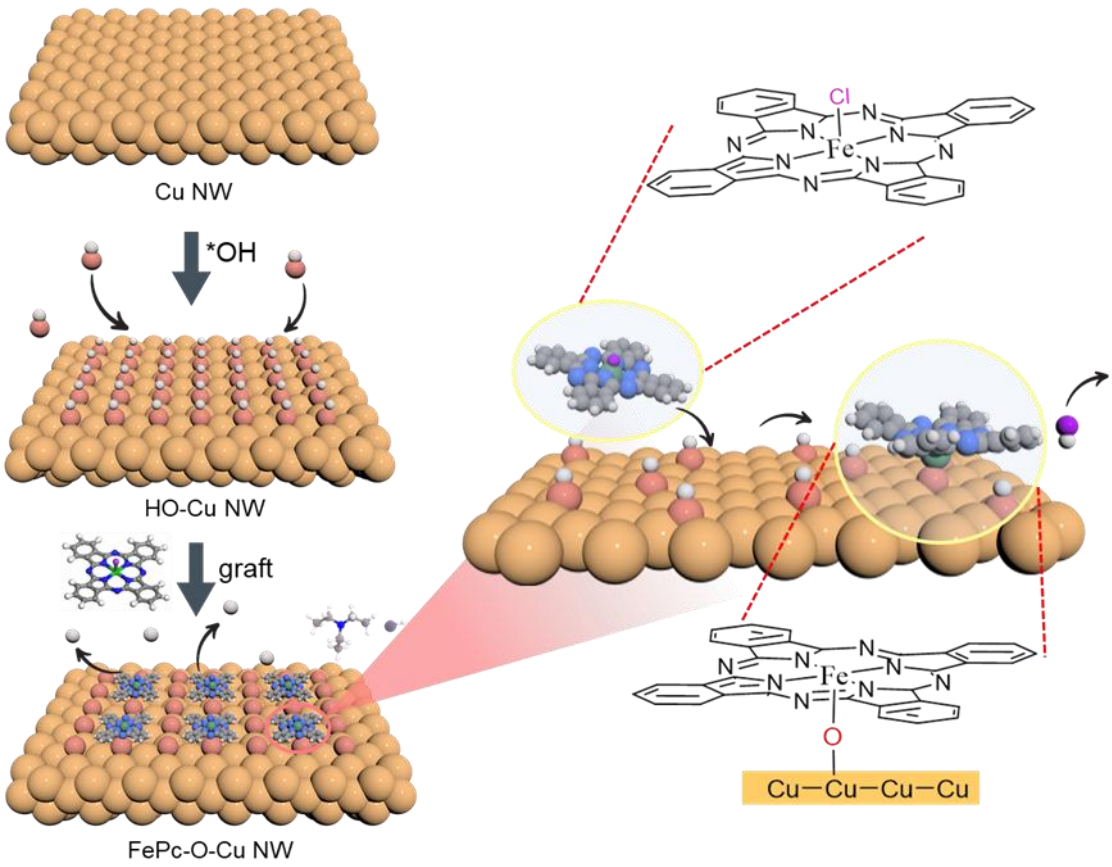

Fig. 1 | Material synthesis. Schematic illustration showing synthesis of FeN_4-O-Cu NW.

The surface valence states of the as-synthesized FeN_4-O-Cu NW, O-Cu NW and reference samples were examined by X-ray photoelectron spectroscopy (XPS). The high-resolution O 1*s* XPS spectra of Cu NW, O-Cu NW, and FeN_4-O-Cu NW show similar characteristic peaks at 531.8 eV, corresponding to adsorbed surface hydroxyl group (OH_{ads}) (Fig. 2d). The enrichment and depletion of surface hydroxyl species over the as-synthesized catalysts reveal the hydroxylation and O-bridging processes during the catalyst synthesis. High-resolution Fe 2*p* XPS spectrum indicates that the oxidation state of the central iron mainly presents a trivalent state in FeN_4-O-Cu NW (Supplementary Fig. 8a). Supplementary Fig. 8 shows that the binding energies of Cu 2*p* and Fe 2*p* shift positively from 932.3 eV (Cu NW) to 932.8 eV (FeN_4-O-Cu NW) and from 712.6 eV (Cl-FePc) to 714.2 eV (FeN_4-O-Cu NW), implying a gradually decreased charge density of Cu/Fe atoms due to electron transfer from

Cu/Fe to O atoms, which may be related to the high electronegativity of oxygen.

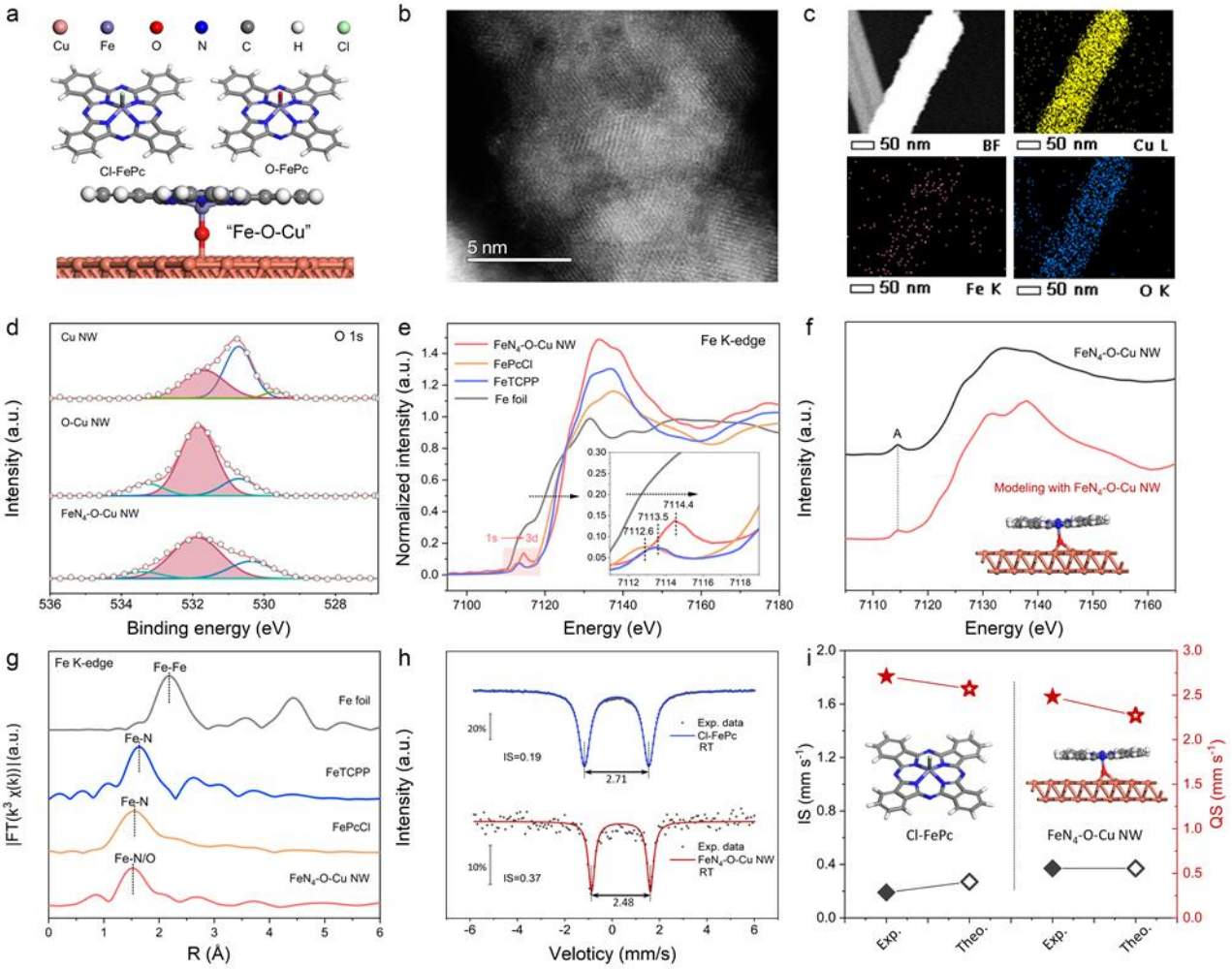

Fig. 2 | Structural characterization. a, Structural models of Cl-FePc, O-FePc and FeN_4-O-Cu NW. **b,** HAADF-STEM (scale bars: 5 nm) image of FeN_4-O-Cu NW. **c,** The EDX elemental mapping images of FeN_4-O-Cu NW. **d**, High-resolution O 1*s* XPS spectra of Cu NW, O-Cu NW and FeN_4-O-Cu NW. **e,** Normalized Fe K-edge XANES spectra of Cl-FePc, FeN_4-O-Cu NW and reference samples (inset shows the enlarged Fe K-edge XANES spectra). **f**, Experimental (black) and simulated (red) Fe K-edge XANES spectra of FeN_4-O-Cu NW. **g**, Fourier transformed Fe K-edge EXAFS spectra of FePcCl, FeN_4-O-Cu NW, and reference samples. **h,** ^{57}Fe Mössbauer spectra of FeN_4-O-Cu NW and Cl-FePc. **i,** Comparison of the experimental IS and QS values of FeN_4-O-Cu NW and Cl-FePc.

X-ray absorption near-edge structure (XANES) and extended X-ray absorption fine structure (EXAFS) analyses were conducted to further elucidate the chemical states and local coordination environments of Cu and Fe in FeN_4-O-Cu NW. As shown in Supplementary Fig. 9a, the Cu K-edge XANES spectra show that the absorption edge of FeN_4-O-Cu NW is close to that for the reference Cu_2O, while the edge feature of FeN_4-O-Cu NW (designated as $1s \rightarrow 3d$ transition) is close to that of the reference commercial Cu foil, suggesting that the Cu atoms in FeN_4-O-Cu NW mainly exist in the form of Cu^0 and Cu^I, matching well with the XPS results. The corresponding EXAFS spectrum and the fitted result of the first coordination shell for FeN_4-O-Cu NW show that the Cu-Cu coordination is located at ~2.23 Å and the Cu-O coordination peak appears at 1.35 Å (Supplementary Fig. 9b). A comparison of the Fe K-edge near-edge absorption energy of FeN_4-O-Cu NW with that of Cl-FePc (Fig. 2e) reveals that the Fe species in FeN_4-O-Cu NW exhibit a higher valence state (Fe (III)), which may be attributed to the stronger electron-withdrawing ability of oxygen atoms relative to chlorine atoms. The pre-edge shift from ~7112.6 eV (Cl-FePc, corresponding to the $1s \rightarrow 3d$ orbital transition) to ~7114.4 eV (FeN_4-O-Cu NW) suggests partial distortion induced by an additional heteroatomic ligand an axially coordinated oxygen atom (Fig. 2e). XANES simulation on the density functional theory (DFT)-optimized FeN_4-O-Cu NW structure shows exceptional consistency between the experimental and theoretical spectrum, further refining the structural understanding of the O-Fe-N_4 moiety, featuring an oxygen atom bonded to the copper NW support as depicted in Fig. 2f. The Fe K-edge EXAFS spectrum of FeN_4-O-Cu NW displays a principal peak at ~1.50 Å, which can be ascribed to Fe-N/O coordination, and the absence of a distinct Fe-Fe scattering peak provides a strong evidence for the uniform dispersion of O-Fe-N_4 species within the as-synthesized FeN_4-O-Cu NW (Fig. 2g).

To further determine the coordination environment, valence and spin state of the single-Fe-atom

species in FeN_4-O-Cu NW, room temperature ^{57}Fe Mössbauer spectroscopy measurements were performed. Only one doublet with the isomer shift (IS) value of 0.37 mm s^{-1} and the quadrupole splitting (QS) value of 2.48 mm s^{-1} was observed (Fig. 2h), which could be unambiguously assigned to LS Fe (III) species (Fig. 2i, Supplementary Table 4). Based on the IS and QS values calculated for a set of hypothetical Fe structures, the fitted parameters of this doublet match well with those calculated by DFT for the optimized FeN_4-O-Cu NW structure (Fig. 2i, Supplementary Figs. 10, 11 and Supplementary Table 5), further confirming the successful synthesis of the model dual-site catalyst with oxygen-bridged Fe-O-Cu sites.

Electrochemical CO_2RR performance

The electrochemical CO_2RR performance was first evaluated in an H-type cell filled with CO_2-saturated 0.1 M $KHCO_3$ electrolyte, and the gas and liquid products were quantified by gas chromatography (GC) and nuclear magnetic resonance (NMR), respectively (Supplementary Figs. 12, 13). For comparison, copper nanowires modified with phthalocyanine iron (FeN_4-Cu NW) without O-bridging were also synthesised. To preliminarily assess the CO_2RR activity of FeN_4-O-Cu NW and FeN_4-Cu NW, linear sweep voltammetry (LSV) measurements were conducted under CO_2 and Ar atmosphere (Fig. 3a), respectively. The LSV curves clearly illustrate that both catalysts exhibit a more positive onset potential and a higher current density under CO_2 atmosphere compared to Ar atmosphere at the same applied potential, indicating that CO_2RR can occur readily rather than the hydrogen evolution reaction (HER) over FeN_4-O-Cu NW and FeN_4-Cu NW, consistent with the cyclic voltammetry (CV) results (Supplementary Fig. 14). Fig. 3b compares the potential-dependent Faradaic efficiencies (FEs) for various CO_2RR products on FeN_4-O-Cu NW and FeN_4-Cu NW. The ethanol Faradaic efficiency ($FE_{ethanol}$) on FeN_4-O-Cu NW displays a volcano-shaped dependence on applied

potential in the range of -0.8 to -1.2 V *vs.* RHE. At -1.0 V *vs.* RHE, FeN_4-O-Cu NW achieves an optimal $FE_{ethanol}$ of 50.4 %, significantly surpassing that of FeN_4-Cu NW, which reaches only 15.9 % at the same potential. Additionally, FeN_4-O-Cu NW demonstrates a maximum ethanol partial current density ($j_{ethanol}$) of 8.9 mA cm^{-2} at -1.0 V *vs*. RHE, compared to 1.6 mA cm^{-2} for FeN_4-Cu NW (Supplementary Fig. 15).

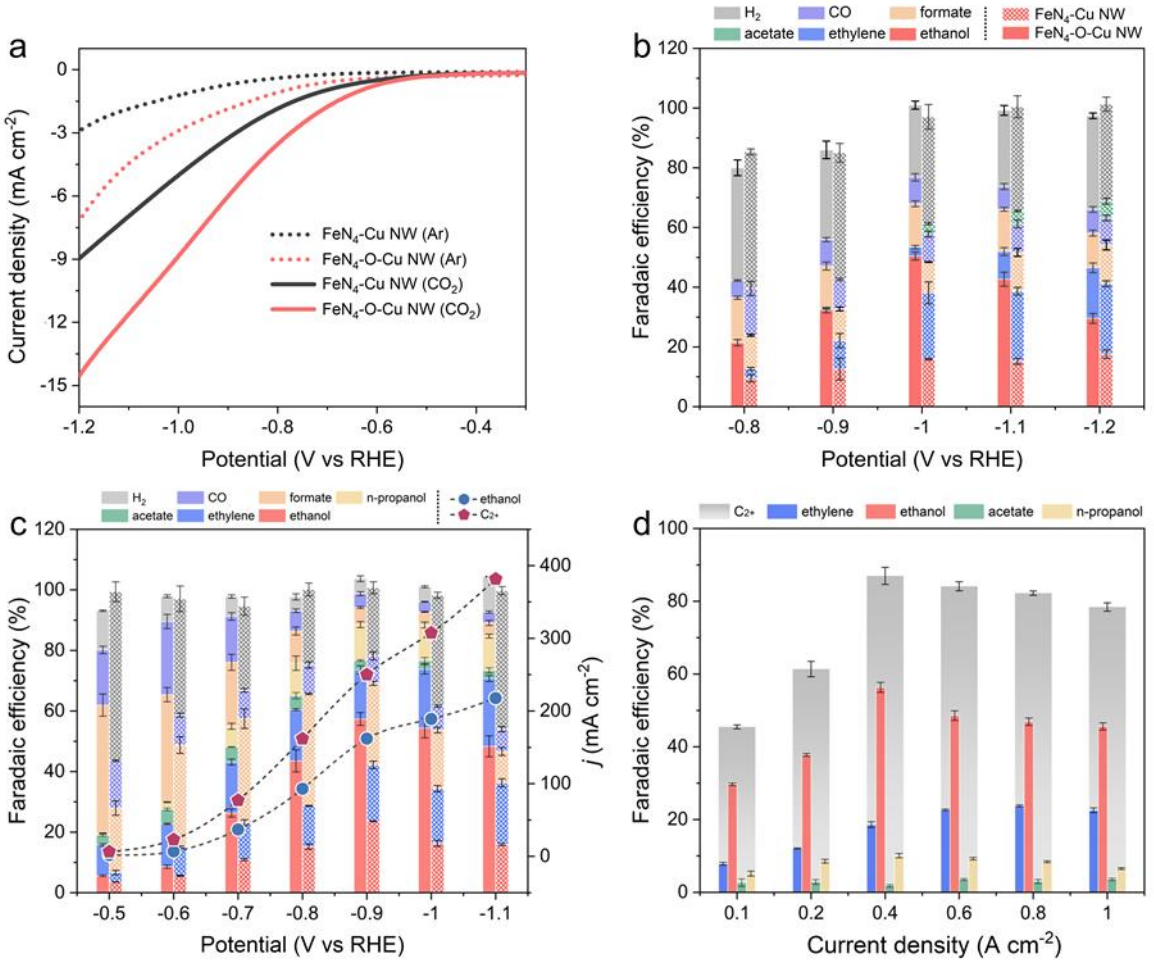

Fig. 3 | Electrochemical CO_2RR performance. a, LSV curves acquired in a CO_2 or Ar-saturated 0.1 M $KHCO_3$ solution on a rotating disc electrode at a rotation speed of 1,600 rpm and a scan rate of 5 mV s^{-1}. **b**, Potential dependent Faradaic efficiencies for CO_2RR on FeN_4-O-Cu NW (left) and FeN_4-Cu NW (right) in an H-type cell. **c**, Potential dependent Faradaic efficiencies recorded over FeN_4-O-Cu NW (left) and FeN_4-Cu NW (right), and current density for CO_2RR to ethanol and C_{2+} products

over FeN_4-O-Cu NW in 1 M KOH electrolyte in a flow cell. Error bars represent the standard deviation of three independent measurements. **d**, Current density dependent Faradaic efficiencies for CO_2RR on FeN_4-O-Cu NW acquired in a flow cell using 1 M KOH as the electrolyte. The results of each potential in Figs. 3b-3d were collected after one hour of continuous electrolysis.

The CO_2RR was further evaluated in a flow-cell electrolyzer to overcome the poor solubility of CO_2 and the sluggish CO_2 mass transport in aqueous solution (Supplementary Fig. 16). As presented in Fig. 3c, CO_2 can be electrochemically reduced to ethanol on FeN_4-O-Cu NW, exhibiting a total current density of 282.5 mA cm^{-2} with an $FE_{ethanol}$ as high as 57.3% at -0.9 V *vs.* RHE (Supplementary Figs. 17, 18). In comparison, FeN_4-Cu NW exhibits a significantly lower FE and partial current density for ethanol production, highlighting the pivotal role of oxygen-bridged Fe-O-Cu sites in facilitating CO_2RR to ethanol. Supplementary Figs. 19 and 20 illustrate the potential-dependent liquid-phase products distribution over FeN_4-O-Cu NW and FeN_4-Cu NW during CO_2RR. Notably, the FeN_4-O-Cu NW catalyst demonstrates an exceptional ethanol selectivity, exhibiting a 23.6-fold enhancement in the ethanol-to-ethylene Faradaic efficiency ratio compared to that of the O-Cu NW (Supplementary Figs. 21, 22). This exceptional performance highlights the critical role of oxygen-bridged Fe-O-Cu sites in promoting selective CO_2-to-ethanol conversion while effectively suppressing the ethylene formation pathway. Fig. 3d displays the FEs of C_{2+} products (ethylene, ethanol, acetate and *n*-propanol) on the FeN_4-O-Cu NW electrode during CO_2RR in the current density range of 100-1000 mA cm^{-2}. An optimal FE for C_{2+} products of 86.9 % can be achieved at a total current density of 400 mA cm^{-2}. Moreover, an FE exceeding 80% for C_{2+} products is achievable at an industrial-relevant current density of 1 A cm^{-2}, which is competitive among the state-of-the-art catalysts reported for electrochemical CO_2 reduction to ethanol (Supplementary Fig. 23, Supplementary Table 6). Besides, negligible decay

in current density and ethanol or C_{2+} products FE are observed during 10 hours of continuous electrolysis (Supplementary Figs. 24), and the FeN_4-O-Cu NW catalyst displays a similar Fe species distribution before and after CO_2RR (Supplementary Fig. 25), suggesting the outstanding catalytic stability of FeN_4-O-Cu NW.

In-situ identification of the catalytic sites for CO_2RR to ethanol

To identify the catalytic sites over FeN_4-O-Cu NW responsible for the CO_2RR to ethanol, *operando* Mössbauer spectroscopy measurements under real operating conditions were carried out (Supplementary Fig. 26). Supplementary Fig. 27 shows the current-time curves recorded during the *operando* Mössbauer spectroscopy measurements. Fig. 4a displays the Mössbauer spectra of FeN_4-O-Cu NW under various applied potentials. Notably, a doublet with an isomer shift (IS) value of 0.35 mm s^{-1} and a quadrupole splitting (QS) value of 2.48 mm s^{-1} was detected over FeN_4-O-Cu NW under open-circuit voltage (OCV) condition, which could be assigned to LS Fe(III). When polarized at -0.6 V *vs.* RHE, negligible changes on IS and QS values were observed as compared to the OCV condition. Starting from -0.9 V *vs.* RHE, the Mössbauer spectra of FeN_4-O-Cu NW revealed a new doublet with IS and QS values of 0.15 and 0.33 mm s^{-1}, which could be attributed to LS Fe (II). Furthermore, the LS Fe (II) became more prominent as the cathodic voltage increased from -0.9 V to -1.2 V *vs*. RHE, while concurrently the relevant LS Fe (III) exhibited a decreasing trend. Supplementary Fig. 28 and Supplementary Table 7 summarize the content variations of all Fe species during CO_2RR at different cathodic potentials. Quantitative analysis indicates that the fraction of LS Fe (II) increases from ~20 % to ~54.1 % as the potential becomes more negative from -0.9 to -1.2 V *vs*. RHE. Moreover, as the applied potential decreases from -0.9 V to -1.2 V *vs*. RHE, the ethanol partial current density gradually increases, aligning well with the trend of the relevant content of LS Fe (II) species, indicating that the

in-situ generated LS Fe (II) over FeN_4-O-Cu NW may play a key role in driving CO_2RR to produce ethanol.

Next, *operando* XANES measurements were conducted to further investigate the dynamic evolution of the FeN_4-O-Cu NW catalyst during CO_2RR. As shown in Fig. 4b, *operando* Cu K-edge XANES spectra were recorded over FeN_4-O-Cu NW at OCV, -0.7 V *vs.* RHE, -1.2 V *vs*. RHE, and AFT (after CO_2RR), respectively. The results indicate that the valence state of Cu in FeN_4-O-Cu NW is maintained close to metallic Cu under various applied cathodic potentials, exhibiting the similar pre-edge and white-line features (marked A, B, C in the XANES spectra of Fig. 4d) as those of Cu foil[38-40]. In detail, at -0.7 V and -1.2 V *vs*. RHE, the Cu K-edge of FeN_4-O-Cu NW was observed shifting to lower energies as compared with that under OCV, indicating reduction of partially oxidized copper NW. This reduction of partially oxidized copper NW was also evident from the FT-EXAFS results, where the peak attributed to Cu-O was converted into Cu-Cu coordination (Supplementary Fig. 29a). Moreover, the FT-EXAFS fitting profiles in the R space, recorded at -0.7 V and -1.2 V *vs.* RHE (Supplementary Fig. 30 and Supplementary Table 8), indicated that although Cu-Cu coordination dominated, some Cu-O coordination still persisted. This suggests that the O-bridged Cu sites originating from Fe-O-Cu can be well maintained during the CO_2RR. A significant left shift in the Fe K-edge XANES spectra (Fig. 4c) suggests that the Fe species in FeN_4-O-Cu NW undergo a continuous reduction as the applied cathodic potential increases from OCV to -1.2 V *vs.* RHE, further confirming the decrease of Fe valence state in FeN_4-O-Cu NW during CO_2RR, matching well with the *operando* Mössbauer results. On the other hand, the FT-EXAFS spectra at the Fe K-edge display only Fe-N/O coordination without the presence of Fe-Fe peak throughout the whole testing period (Supplementary Fig. 29b), indicating that Fe species are always distributed in the form of single atoms during the

CO_2RR process.

Quasi in-situ XPS measurements were performed to precisely track the oxidation state of surficial Cu species on FeN_4-O-Cu NW during CO_2RR (Supplementary Fig. 31). As displayed in Supplementary Fig. 32, the *quasi in-situ* XPS spectra recorded on O-Cu NW indicate a continuous reduction of surficial Cu with increasing applied cathodic potential, as evidenced by the progressive decrease of the Cu^+/Cu^0 ratio from 1.08 to 0.15 (Supplementary Table 9). For FeN_4-O-Cu NW, as shown in Fig. 4d, the high-resolution *quasi in-situ* Cu 2*p* XPS spectra reveal that the Cu species on FeN_4-O-Cu NW surface consist of both Cu^{2+} and $Cu^{0/+}$ under OCV condition. Upon increasing the cathodic potential to -0.7 V *vs.* RHE, the Cu^{2+} signals disappear rapidly. Furthermore, the Cu 2*p* XPS spectra maintain similar $Cu^{0/+}$ profiles from -0.7 to -1.1 V *vs.* RHE. To differentiate $Cu^{0/+}$, Auger spectroscopy measurements were conducted (Fig. 4e). Quantitative XPS analysis demonstrates that the FeN_4-O-Cu NW surface initially contains Cu^0, Cu^+, and Cu^{2+} species under open-circuit condition. Increasing applied cathodic potential cause complete reduction of Cu^{2+}, yielding exclusively Cu^0/Cu^+ species. Remarkably, unlike O-Cu NW, the FeN_4-O-Cu NW can maintain a stable Cu^+/Cu^0 ratio under various cathodic potential conditions, demonstrating the outstanding structural integrity of the oxygen-bridged Fe-O-Cu moieties during CO_2RR (Supplementary Table 9).

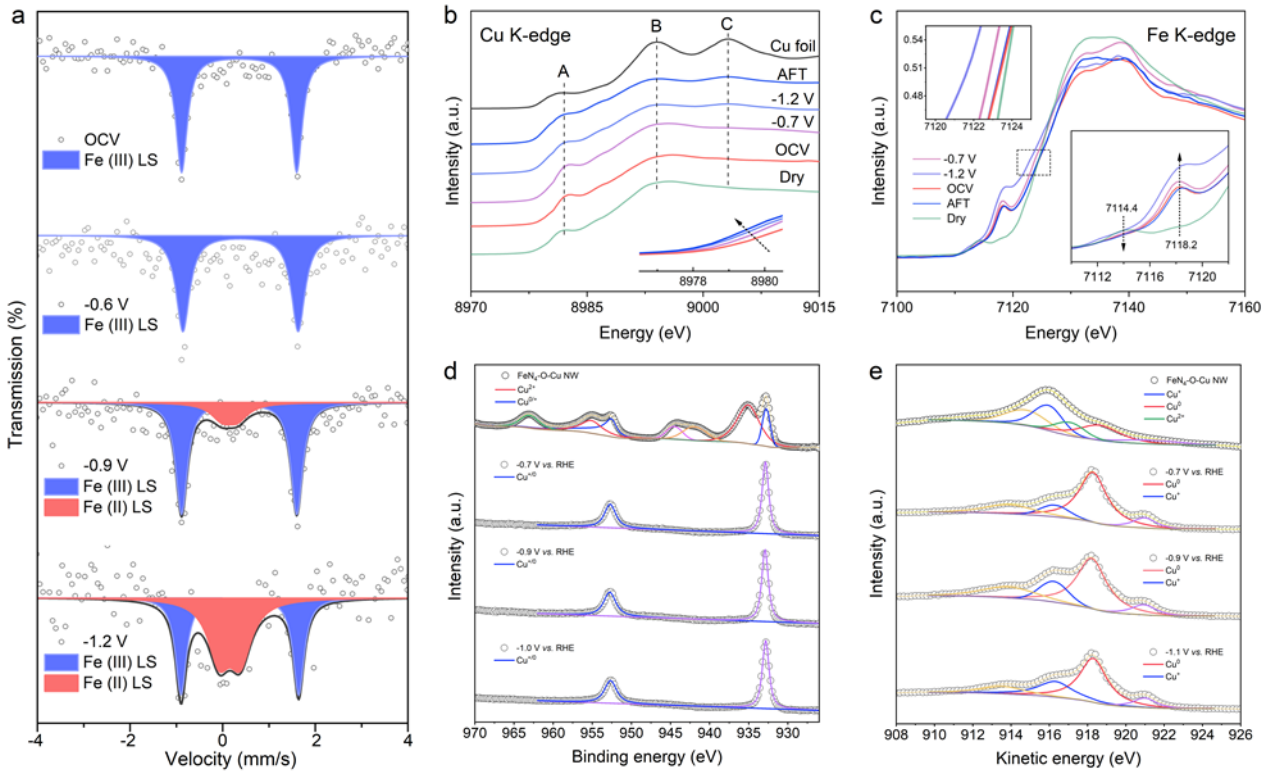

Fig. 4 | Dynamic evolution of FeN_4-O-Cu NW during CO_2RR. a, *Operando* ^{57}Fe Mössbauer spectra of ^{57}Fe-enriched FeN_4-O-Cu NW recorded at OCV, -0.6 V *vs*. RHE, -0.9 V *vs*. RHE, and -1.2 V *vs*. RHE in CO_2-saturated 0.1 M $KHCO_3$ electrolyte. **b**, **c**, Normalized *operando* Cu and Fe K-edge XANES spectra of FeN_4-O-Cu NW recorded at OCV, -0.7 V *vs*. RHE, -1.2 V *vs*. RHE, and AFT in CO_2-saturated 0.1 M $KHCO_3$ electrolyte. High-resolution *quasi in-situ* (**d**) Cu 2*p* XPS spectra and (**e**) Cu Auger spectra of FeN_4-O-Cu NW recorded at OCV, -0.7 to -1.1 V *vs.* RHE (ΔE = 0.2 V) in CO_2-saturated 0.5 M $KHCO_3$ electrolyte.

Mechanistic insights

To probe the CO_2RR to ethanol pathway, *operando* ATR-SEIRAS measurements were conducted at various applied cathodic potentials (Supplementary Fig. 33). Figs. 5a, 5b, and Supplementary Fig. 34 present the *operando* ATR-SEIRAS spectra recorded on FeN_4-O-Cu NW and FeN_4-Cu NW in CO_2-saturated 0.5 M $KHCO_3$ electrolyte. A distinct H_2O absorption peak at around 1620 cm^{-1} was observed

on both catalysts[41,42]. However, on FeN_4-O-Cu NW, the H_2O absorption peak is noticeably less pronounced as compared to that on FeN_4-Cu NW, indicating that the oxygen bridging effect can effectively suppress water adsorption on FeN_4-O-Cu NW, which may help to reduce the undesired HER over FeN_4-O-Cu NW. When the applied cathodic potential increased to -0.3 V *vs.* RHE, two distinct peaks emerged at ~2050 and 1865 cm^{-1} over FeN_4-O-Cu NW, corresponding to *CO species adsorbed in the atop ($*CO_{atop}$) and bridge ($*CO_{bridge}$) configurations on the catalyst's surface (Figs. 5a, 5b, Supplementary Table 10)[43-45]. The ratio of $*CO_{bridge}/*CO_{atop}$ over FeN_4-O-Cu NW is much larger than that over FeN_4-Cu NW (Fig. 5c). Between the two types of *CO species, the $*CO_{bridge}$ intermediate can more readily participate in the hydrogenation reaction due to its comparatively weaker C=O bond as compared to $*CO_{atop}$[11,46]. The stronger *OCHO peak (~1367 cm^{-1}) observed on FeN_4-O-Cu NW indicates enhanced CO_2 activation compared to that on FeN_4-Cu NW. Additionally, new peaks at around 1244 cm^{-1} and 1083 cm^{-1} are observed on FeN_4-O-Cu NW, which can be assigned to the adsorbed *CHO and *COCHO intermediates, respectively (Fig. 5a). In addition, the peak intensity of *COCHO intermediate gradually increased as the applied cathodic potential was raised from -0.3 to -1.6 V *vs.* RHE, while the peak intensity of *CHO intermediate was correspondingly decreased (Fig. 5d). This observation suggests that the *COCHO intermediate is formed *via* asymmetric coupling between *CO and *CHO. The *operando* ATR-SEIRAS spectra of the KSCN-poisoned FeN_4-O-Cu NW did not reveal any peaks associated with the *CO intermediate, further confirming that the single-atom Fe sites served as the active centers for *CO production during the CO_2RR process (Fig. 5f and Supplementary Fig. 35). Additionally, after poisoning the single-atom Fe sites with KSCN, the LSV curves of FePcCl and FeN_4-O-Cu NW exhibited a sharp decrease in current density under CO_2 atmosphere, indicating that the single-atom Fe centers are essential for the CO_2RR

(Fig. 5e). Meanwhile, the CO Faradaic efficiency of Cl-FePc and the ethanol Faradaic efficiency of FeN_4-O-Cu NW both decreased significantly (Supplementary Figs. 36, 37). All these results support our hypothesis that the *CO intermediate species generated at the single-atom Fe sites and the asymmetric coupling between *CO and *CHO (derived from *OCHO) over oxygen-bridged Fe-O-Cu sites should be responsible for ethanol production *via* CO_2RR over FeN_4-O-Cu NW.

For the CO_2RR to mulicarbon products, the conversion of CO_2-to-CO and subsequently CO-to-C_{2+} products are typically considered a sequential two-step process, with each step requiring distinct catalytic sites. Consequently, the electrochemical CO reduction reaction (CORR) has frequently been employed as a model reaction to elucidate the reaction pathways leading to the C_{2+} products formation in CO_2RR. As shown in Fig. 5g, the potential-dependent FE values of different CORR products obtained on FeN_4-O-Cu NW, using CO as the feed gas, illustrate a significant difference in dominant products compared to CO_2RR. The FE of acetate over FeN_4-O-Cu NW reached as high as 78.6 % at -1.0 V *vs.* RHE. Given the distinct product distributions of FeN_4-O-Cu NW in CO_2RR and CORR, co-electrolysis of CO_2 + CO mixtures with varying ratios was conducted in 1 M KOH at -1.0 V *vs*. RHE to examine the influence of feed composition on reaction kinetics and product selectivity. As shown in Figs. 5h, i and Supplementary Fig. 38, a lower CO_2 ratio in the co-feed leads to a decline in $FE_{ethanol}$, while $FE_{acetate}$ raises when the CO concentration is increased. This variation in product distribution likely arises from competition between CO_2RR- and CORR-derived intermediates for catalytic sites, suggesting that ethanol formation is strongly dependent on CO_2-derived intermediates.

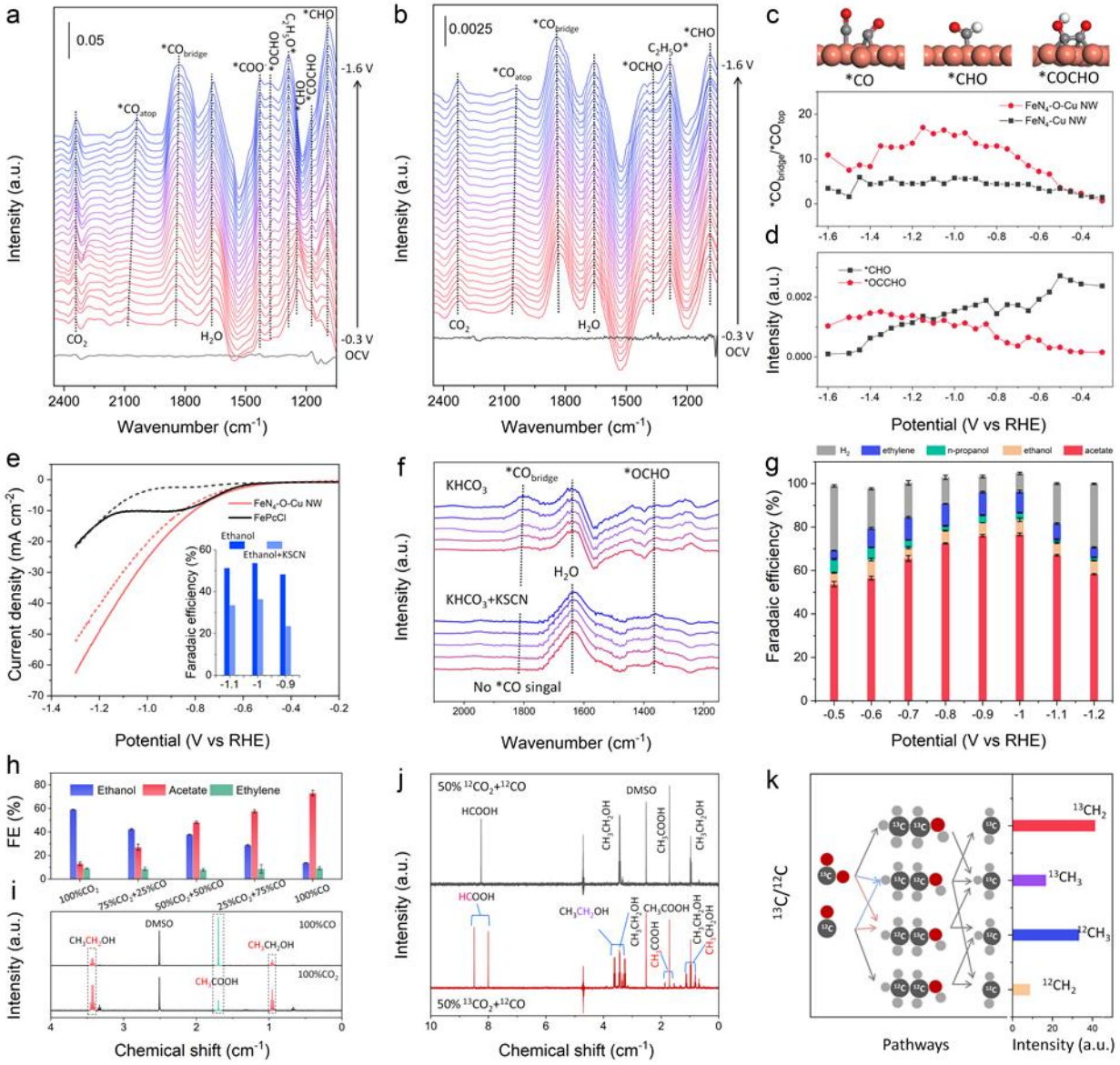

Fig. 5 | Reaction mechanism. a, **b**, *Operando* ATR-SEIRAS spectra recorded in CO_2-saturated 0.1 M $KHCO_3$ solution at various potentials (V *vs.* RHE) over FeN_4-O-Cu NW and FeN_4-Cu NW, respectively. Potential-dependent ATR-SEIRAS peak intensity for (**c**) $*CO_{atop}/*CO_{bridge}$ and (**d**) *CHO with *OCCHO intermediate over FeN_4-O-Cu NW. e, LSV curves acquired in CO_2-saturated 0.5 M $KHCO_3$ solution with or without KSCN over Cl-FePc and FeN_4-O-Cu NW (inset shows $FE_{ethanol}$ of FeN_4-O-Cu NW). **f**, *Operando* ATR-SEIRAS spectra recorded in CO_2-saturated 0.1 M $KHCO_3$ solution with or without KSCN at various potentials (V *vs.* RHE) over FeN_4-O-Cu NW. **g**, Potential

dependent Faradaic efficiencies for CORR on FeN_4-O-Cu NW in 1 M KOH electrolyte (flow cell). Error bars represent the standard deviation of three independent measurements. **h**, Faradaic efficiencies of C_2 products for CO_2RR under different CO_2/CO ratios recorded on FeN_4-O-Cu NW at -1.0 V *vs.* RHE. **i**, ^{1}H NMR spectra of the electrolyte after electrolysis (E = -1.0 V *vs.* RHE, t = 1 h) in 100%CO_2 and 100%CO-saturated solutions. **j**, ^{1}H NMR spectra of the electrolyte after electrolysis (E = -1.0 V *vs.* RHE, t = 1 h) in 100% $^{12}CO_2/^{13}CO_2$ and 50% $^{12}CO_2/^{13}CO_2$+^{12}CO-saturated electrolyte. **k**, The distribution and abundance statistics of $^{13}C/^{12}C$ in ethanol product.

To probe the origin of carbon species in ethanol product, electrolysis was performed using isotope labelled CO_2/CO. Fig. 5j and Supplementary Fig. 39 show the ^{1}H NMR spectra of ethanol produced from pure $^{13}CO_2$ feed, pure ^{12}CO feed and $^{13}CO_2$ + ^{12}CO co-feed. As presented in Supplementary Fig. 39, isotope labelling experiments using 100% $^{13}CO_2$ and 100% ^{13}CO as reactants yield products entirely labelled with ^{13}C, including ethanol, acetate, and formate, confirming that the carbon in the feed gas serves as the exclusive carbon source for the target products. Co-electrolysis of $^{13}CO_2$ + ^{12}CO (1:1) further supports the hypothesis that CO_2 has a promotional effect on the CO_2RR to ethanol. The ^{1}H NMR result from the $^{13}CO_2$ + ^{12}CO co-feed experiment reveals four types of ethanol products: $^{13}CH_3{}^{12}CH_2OH$, $^{12}CH_3{}^{13}CH_2OH$, $^{12}CH_3{}^{12}CH_2OH$, and $^{13}CH_3{}^{13}CH_2OH$ (Fig. 5k). Notably, the peak area for CH_2 in ^{13}C-labelled ethanol is significantly larger than that for CH_3, and quantitative analysis of the peak areas shows the following relative abundance: $^{13}CH_2 > {}^{12}CH_3 > {}^{13}CH_3 > {}^{12}CH_2$, suggesting that the coupling of *CO with *CHO (derived from hydrogenation of CO_2 to *OCHO) is crucial for ethanol formation *via* CO_2RR over FeN_4-O-Cu NW.

Theoretical insights

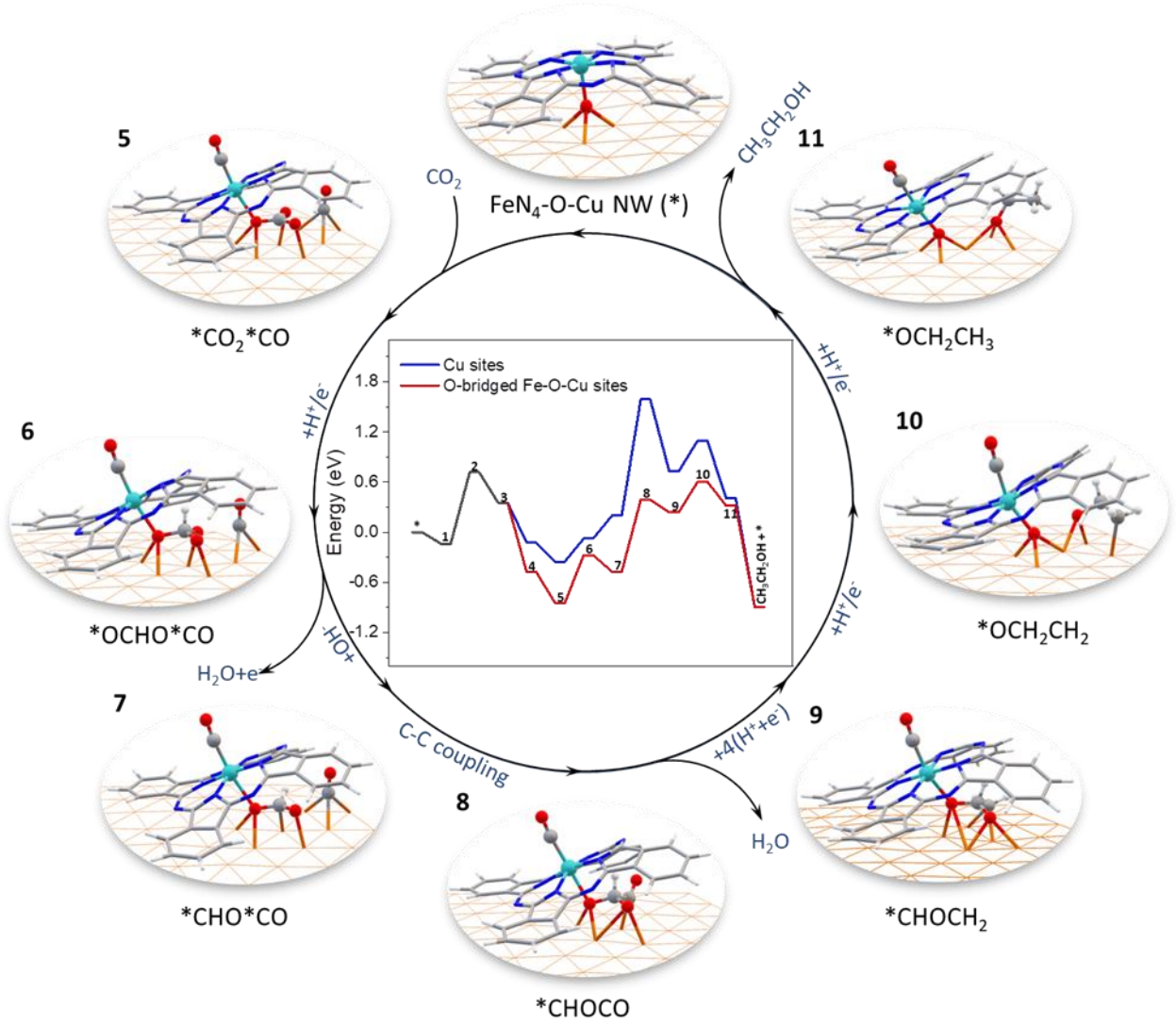

Fig. 6 | DFT calculations. Calculated Gibbs free energy profiles and optimized intermediate structures illustrating the CO_2RR pathway to ethanol over the FeN_4-O-Cu NW catalyst. See Supplementary Figs. 40 and 41 for steps 1 to 4.

Based on the above experimental results, DFT calculations were performed to gain theoretical insights into the underlying reaction mechanism of CO_2RR to ethanol over FeN_4-O-Cu NW. The related optimized configurations of the potential reaction intermediates involved the ethanol pathways of CO_2RR over FeN_4-O-Cu NW are shown in Supplementary Figs. 40-42. Combined with *operando* ATR-SEIRAS measurements and probe experiments (KSCN-poisoning and $^{13}CO_2$ + ^{12}CO co-feed

experiments), it is deduced that both the Fe single-atom sites and the O-bridged Cu sites are involved in the synthesis of ethanol *via* CO_2RR over FeN_4-O-Cu NW. Therefore, the energy barriers for the *CO production at the single-atom Fe sites and the C-C coupling at the O-bridged Cu sites were calculated and the results are displayed in Fig. 6. As shown, the reaction free energy for the conversion of CO_2 to *COOH (step **1**→**2**, the rate-determining step, RDS) on the LS Fe (II) site is 0.85 eV, indicating enhanced CO_2RR toward CO generation (Supplementary Fig. 37). Given the pivotal role of O-bridged Fe-O-Cu sites in ethanol production *via* CO_2RR, we conducted a comparative investigation into the two distinct CO_2 binding mechanisms on oxygen-bridged Cu sites and pristine Cu sites. The results reveal that O-bridged Cu sites, where both O and Cu atoms synergistically bond CO_2 (step **4**) to form *OCHO, realize a significantly lower Gibbs free energy (-0.47 eV) compared to pristine Cu sites (-0.12 eV). Additionally, the lower *OCHO-to-*CHO conversion energy barrier (step **6**→**7**, -0.20 eV) on O-bridged Cu sites can further promote *CHO formation. Therefore, the C-C coupling step in ethanol formation is proposed to proceed through the interaction of *CHO species (generated *via* protonation and dehydration of the *OCHO intermediate at O-bridged Cu sites) with *CO species (produced at LS Fe(II) sites and transferred to Cu), forming the *CHOCO dimeric intermediate (step **7**→**8**, 0.86 eV), which is well consistent with the results from multiple *operando*/*in-situ* characterizations and $^{13}CO_2$ + ^{12}CO co-feed experiments.

On the basis of the above results, the CO_2RR to ethanol mechanism over FeN_4-O-Cu NW is clearly elucidated (Fig. 6). The ethanol pathway proceeds through the asymmetric C-C coupling of *CO intermediates produced at the LS Fe(II) sites and *CHO intermediates generated at the O-bridged Cu sites. The rationally constructed O-bridged Fe-O-Cu sites can not only facilitate efficient *CO release from LS Fe(II) sites but also markedly reduce the Gibbs free energy barrier for the *OCHO-to-*CHO

conversion on oxygen-bridged Cu sites, thereby enabling preferential and efficient CO_2 reduction to ethanol through asymmetric *CO-*CHO coupling.

CONCLUSIONS

In summary, we have successfully developed FeN_4-O-Cu NW with precisely configured Fe-O-Cu sites, achieving a maximum $FE_{ethanol}$ of 57.3% at -0.9 V *vs*. RHE with an ethanol partial current density of 282.5 mA cm^{-2}, and an over 80% Faradaic efficiency for C_{2+} products at an industrial current density of 1 A cm^{-2} in CO_2RR. Results from *operando* XAS and ^{57}Fe Mössbauer spectroscopy measurements have clearly tracked the dynamic evolution of single-Fe-atom sites from LS Fe(III) to LS Fe(II) during CO_2RR over FeN_4-O-Cu NW. *Quasi in-situ* XPS results demonstrate a direct correlation between the Cu^+/Cu^0 ratio and ethanol Faradaic efficiency, indicating that the O-bridged Fe-O-Cu sites should be essential for the selective CO_2-to-ethanol conversion. Following a combination of $^{13}CO_2$ + ^{12}CO co-feed experiments and *operando* ATR-SEIRAS measurements, the enhanced ethanol selectivity over FeN_4-O-Cu NW arises from asymmetric C-C coupling between *CO and *CHO, where *CO species are produced at the *in-situ* generated LS Fe(II) sites, and *CHO species are formed at the O-bridged Cu sites. Theoretical calculations further demonstrate that the Fe-O-Cu sites can not only reduce the *CO desorption energy barrier at the *in-situ* generated LS Fe(II) sites, but also stabilize the *OCHO intermediate at the O-bridged Cu sites, reducing the *OCHO-to-*CHO conversion energy barrier, which collectively enable an efficient asymmetric *CO-*CHO coupling process, thus greatly boosting electrochemical CO_2 reduction to ethanol. The results of this work provide clear insights into the asymmetric C-C coupling pathway for electrochemical CO_2 reduction to ethanol and shall pave the way for the rational design of novel electrocatalysts with dual active sites for efficient CO_2RR.

Acknowledgments

This work was financially supported by the Strategic Priority Research Program of the Chinese Academy of Sciences (XDB0600200 (X.L.)), the National Key Research and Development Program of China (No. 2021YFA1500502 (X.L.)), the NSFC Center for Single-Atom Catalysis (grant No. 22388102 (X.L.)), the National Natural Science Foundation of China (22478377 (X.L.)), the National Natural Science Foundation of China Youth Science Fund Project (22402188 (J.Z.)), CAS Project for Young Scientists in Basic Research (YSBR-051 (X.L.)), the DICP.CAS-Cardiff Joint Research Units (121421ZYLH20230008 (X.L.)), the City University of Hong Kong Startup fund (9020003 (B.L.)), ITF-RTH-Global STEM Professorship (9446006 (B.L.)), JC STEM lab of Advanced CO_2 Upcycling (9228005 (B.L.)), and the Liaoning Foundation for Excellent Young Scholars (2025JH6/101000018). The authors gratefully acknowledge the support of Photon Science Center for Carbon Neutrality. We thank the Shanghai Synchrotron Radiation Facility of BL14W1(https://cstr.cn/31124.02.SSRF.BL14W1) for the assistance on XAFS measurements.

Author Contribution Statement

S.W., X.L., Y.H. and B.L. designed and conceived the experiment. S.W. performed the catalyst synthesis, structural characterization, and CO_2RR electrocatalytic measurements. J.Z. and X.L. conducted the theoretical calculations. S.W. and Y.Z performed the *operando* electrochemical ATR-SEIRAS measurements and analyses. S.W., Y.L. and W.X. contributed to the *operando* XAS spectroscopy measurements and analyses. S.W., Y.Z. and X.L. performed the *operando* ^{57}Fe Mössbauer spectroscopy measurements and analyses. W.W. performed the HAADF-STEM measurements and analyses. S.W., X.L., O.A. and B.L. wrote and revised the manuscript with inputs from all authors. The project was supervised by X.L., Y.H., G.H., B.L. and T.Z.

Conflict of interest

The authors declare no competing interests.

Data availability

The *ex-situ* XPS data, *ex-situ* XAS data, product quantification, *quasi in-situ* XPS data, *operando* XAS data, *operando* ATR-SEIRAS data, isotope labelling experiments data and theoretical calculations data generated in this study have been deposited in the Figshare database under accession code (https://doi.org/10.6084/m9.figshare.27199515).

References

1 Kazlou, T., Cherp, A. & Jewell, J. Feasible deployment of carbon capture and storage and the requirements of climate targets. *Nat. Clim. Change* **14**, 1047-1055 (2024).

2 Rau, G. H., Willauer, H. D. & Ren, Z. J. The global potential for converting renewable electricity to negative-CO_2-emissions hydrogen. *Nat. Clim. Change* **8**, 621-625 (2018).

3 Lu, X. *et al.* Visualization of CO_2 electrolysis using optical coherence tomography. *Nat. Chem.* **16**, 979-987 (2024).

4 Wu, Y., Jiang, Z., Lu, X., Liang, Y. & Wang, H. Domino electroreduction of CO_2 to methanol on a molecular catalyst. *Nature* **575**, 639-642 (2019).

5 Xu, Z. *et al.* Electroreduction of CO_2 to methane with triazole molecular catalysts. *Nat. Energy* **9**, 1397-1406 (2024).

6 Su, J. *et al.* Strain enhances the activity of molecular electrocatalysts via carbon nanotube supports. *Nat. Catal.* **6**, 818-828 (2023).

7 Xue, J. *et al.* Turning copper into an efficient and stable CO evolution catalyst beyond noble metals. *Nat. Commun.* **15**, 5998 (2024).

8 Zhang, J. *et al.* Isotopic labelling of water reveals the hydrogen transfer route in electrochemical CO_2 reduction. *Nat. Chem.* **17**, 334-343 (2025).

9 Zhan, C. *et al.* Key intermediates and Cu active sites for CO_2 electroreduction to ethylene and ethanol. *Nat. Energy* **9**, 1485-1496 (2024).

10 Cai, Y. *et al.* Self-pressurizing nanoscale capsule catalysts for CO_2 electroreduction to acetate or propanol. *Nat. Synth.* **3**, 891-902 (2024).

11 Ding, J. *et al.* Molecular tuning boosts asymmetric C-C coupling for CO conversion to acetate. *Nat. Commun.* **15**, 3641 (2024).

12 Seger, B., Robert, M. & Jiao, F. Best practices for electrochemical reduction of carbon dioxide. *Nat. Sustain.* **6**, 236-238 (2023).

13 Wang, M. *et al.* Enhanced intermediates inter-migration on Ag single-atom alloys for boosting multicarbon product selectivity in CO_2 electroreduction. *J. Am. Chem. Soc.* **147**, 16450-16458 (2025).

14 Liang, Y. *et al.* Efficient ethylene electrosynthesis through C–O cleavage promoted by water

dissociation. *Nat. Synth.* **3**, 1104-1112 (2024).

15 Wang, S. *et al.* Manipulating C-C coupling pathway in electrochemical CO_2 reduction for selective ethylene and ethanol production over single-atom alloy catalyst. *Nat. Commun.* **15**, 10247 (2024).

16 Karapinar, D. *et al.* Electroreduction of CO_2 on single-site copper-nitrogen-doped carbon material: selective formation of ethanol and reversible restructuration of the metal sites. *Angew. Chem. Int. Ed. Engl.* **58**, 15098-15103 (2019).

17 Wei, P. *et al.* Coverage-driven selectivity switch from ethylene to acetate in high-rate CO_2/CO electrolysis. *Nat. Nanotechnol.* **18**, 299-306 (2023).

18 Jin, J. *et al.* Constrained C_2 adsorbate orientation enables CO-to-acetate electroreduction. *Nature* **617**, 724-729 (2023).

19 Xie, Y. *et al.* High carbon utilization in CO_2 reduction to multi-carbon products in acidic media. *Nat. Catal.* **5**, 564-570 (2022).

20 Jiawei Zhang *et al.* Steering CO_2 electroreduction pathway toward ethanol via surface-bounded hydroxyl species-induced noncovalent interaction. *PNAS* **120**, e2218987120 (2023).

21 Qiao, Y. *et al.* Interfacial oxygen vacancy-copper pair sites on inverse CeO_2/Cu catalyst enable efficient CO_2 electroreduction to ethanol in acid. *Angew. Chem. Int. Ed. Engl.* **64**, e202424248 (2025).

22 Yang, B. *et al.* Accelerating CO_2 electroreduction to multicarbon products via synergistic electric–thermal field on copper nanoneedles. *J. Am. Chem. Soc.* **144**, 3039-3049 (2022).

23 Zhang, Y. *et al.* Low-coordinated copper facilitates the $*CH_2CO$ affinity at enhanced rectifying interface of Cu/Cu_2O for efficient CO_2-to-multicarbon alcohols conversion. *Nat. Commun.* **15**, 5172 (2024).

24 Gao, X. *et al.* Intermediate-regulated dynamic restructuring at Ag-Cu biphasic interface enables selective CO_2 electroreduction to C_{2+} fuels. *Nat. Commun.* **15**, 10331 (2024).

25 Xiao, Y. *et al.* Asymmetric CO-CHO coupling over Pr single-atom alloy enables industrial-level electrosynthesis of ethylene. *J. Am. Chem. Soc.* **147**, 15654-15665 (2025).

26 Zhong, D. *et al.* Selective electrochemical CO_2 reduction to ethylene or ethanol via tuning *OH adsorption. *Angew. Chem. Int. Ed. Engl.* e202501773 (2025).

27 Qiao, B. *et al.* Single-atom catalysis of CO oxidation using Pt_1/FeO_x. *Nat. Chem.* **3**, 634-641 (2011).

28 Shi, X. *et al.* Metal–support frontier orbital interactions in single-atom catalysis. *Nature* **640**, 668-675 (2025).

29 Abdinejad, M. *et al.* Eliminating redox-mediated electron transfer mechanisms on a supported molecular catalyst enables CO_2 conversion to ethanol. *Nat. Catal.* **7**, 1109-1119 (2024).

30 Nam, D.-H. *et al.* Molecular enhancement of heterogeneous CO_2 reduction. *Nat. Mater.* **19**, 266-276 (2020).

31 Li, F. *et al.* Cooperative CO_2-to-ethanol conversion via enriched intermediates at molecule–metal catalyst interfaces. *Nat. Catal.* **3**, 75-82 (2019).

32 Zhang, J. *et al.* Accelerating electrochemical CO_2 reduction to multi-carbon products via asymmetric intermediate binding at confined nanointerfaces. *Nat. Commun.* **14**, 1298 (2023).

33 Liu, C. *et al.* Nanoconfinement engineering over hollow multi-shell structured copper towards efficient electrocatalytical C−C coupling. *Angew. Chem. Int. Ed. Engl.* **61**, e202113498 (2021).

34 Jiao, J. *et al.* Copper atom-pair catalyst anchored on alloy nanowires for selective and efficient electrochemical reduction of CO_2. *Nat. Chem.* **11**, 222-228 (2019).

35 Kim, J.-Y. *et al.* Selective hydrocarbon or oxygenate production in CO_2 electroreduction over metallurgical alloy catalysts. *Nat. Synth.* **3**, 452-465 (2023).

36 Somashekarappa, M. P., Keshavayya, J. & Sherigara, B. S. Synthesis and spectroscopic investigations of iron(III) complexes with chlorides and dianionic, symmetrically halogen substituted phthalocyanines as ligands. *Spectrochim. Acta A* **59**, 883-893 (2003).

37 Zeng, Y. *et al.* Unraveling the electronic structure and dynamics of the atomically dispersed iron sites in electrochemical CO_2 reduction. *J. Am. Chem. Soc.* **145**, 15600-15610 (2023).

38 Yang, B. *et al.* Electrocatalytic CO_2 reduction to alcohols by modulating the molecular geometry and Cu coordination in bicentric copper complexes. *Nat. Commun.* **13**, 5122 (2022).

39 Arán-Ais, R. M., Scholten, F., Kunze, S., Rizo, R. & Roldan Cuenya, B. The role of in situ generated morphological motifs and Cu(i) species in C_{2+} product selectivity during CO_2 pulsed electroreduction. *Nat. Energy* **5**, 317-325 (2020).

40 Jiao, J. *et al.* Steering the reaction pathway of CO_2 electroreduction by tuning the coordination number of copper catalysts. *J. Am. Chem. Soc.* **146**, 15917-15925 (2024).

41 Gao, W., Xu, Y., Fu, L., Chang, X. & Xu, B. Experimental evidence of distinct sites for CO_2-to-CO and CO conversion on Cu in the electrochemical CO_2 reduction reaction. *Nat. Catal.* **6**, 885-

894 (2023).

42 Zhu, Q. *et al.* The solvation environment of molecularly dispersed cobalt phthalocyanine determines methanol selectivity during electrocatalytic CO_2 reduction. *Nat. Catal.* **7**, 987-999 (2024).

43 Liang, Y. *et al.* Stabilizing copper sites in coordination polymers toward efficient electrochemical C-C coupling. *Nat. Commun.* **14**, 474 (2023).

44 Fu, W. *et al.* Preserving molecular tuning for enhanced electrocatalytic CO_2-to-ethanol conversion. *Angew. Chem. Int. Ed. Engl.* **63**, e202407992 (2024).

45 Yoo, S. *et al.* Excess cations alter *CO intermediate configuration and product selectivity of Cu in acidic electrochemical CO_2 reduction reaction. *J. Am. Chem. Soc.* **147**, 12996-13007 (2025).

46 Bai, H. *et al.* Controllable CO adsorption determines ethylene and methane productions from CO_2 electroreduction. *Sci. Bull.* **66**, 62-68 (2021).